

# Consideration of rupture kinematics increases tsunami amplitudes in far-field hazards assessments

Diego Melgar  \* 1,2

<sup>1</sup>Department of Earth Sciences, University of Oregon, Eugene, OR, USA, <sup>2</sup>Cascadia Region Earthquake Science Center, Eugene, OR, USA

Author contributions: *Conceptualization*: D. Melgar. *Methodology*: D. Melgar. *Software*: D. Melgar.

**Abstract** Tsunami hazard assessments often assume that co-seismic crustal deformation occurs instantaneously, particularly in probabilistic tsunami hazard analyses (PTHA). However, this simplification neglects the kinematics of rupture propagation, which may influence tsunami amplitudes at distant sites. Building on previous work, this study investigates the impact of rupture kinematics—specifically rupture directivity and duration—on far-field tsunami amplitudes. Using 2,600 synthetic megathrust earthquake scenarios along a 1,500 km segment of the Alaskan subduction zone, I model tsunami propagation with both instantaneous and time-dependent rupture assumptions. Simulations reveal that source kinematics can significantly rotate the tsunami radiation pattern and increase peak amplitudes by over 30% at far-field sites for large ( $M_w > 9.0$ ) events. When incorporated into a full PTHA framework, the inclusion of rupture kinematics systematically increases hazard estimates at most coastal locations. These results suggest that neglecting rupture kinematics may lead to underestimation of far-field tsunami hazard, particularly for large, unilateral ruptures. I recommend the formal inclusion of rupture kinematics in both deterministic scenario design and probabilistic hazard frameworks to better capture the full range of potential tsunami impacts.

**Non-technical summary** Tsunamis are large surges of sea water caused by undersea earthquakes. To prepare for future tsunamis, scientists run computer simulations to estimate how big the waves might be and how often they could happen. These simulations are used to make maps and design buildings that can withstand tsunami impacts. Most of these models assume that when an earthquake breaks a fault this happens all at once. But in reality, earthquakes unfold over time—sometimes taking several minutes to rupture hundreds of miles of fault. This study shows that the way an earthquake a fault (called "rupture kinematics") can change the size and timing of the tsunami waves that reach faraway places, like Hawaii or the U.S. West Coast. By modeling thousands of possible earthquakes along Alaska's subduction zone, we found that accounting for the way earthquakes move along the fault can make the tsunami waves significantly larger—especially for very big earthquakes. In some cases, ignoring this time evolution could underestimate the impacts by 30% or more. This means current tsunami hazard assessments may be biased low. To better prepare for future tsunamis, we recommend updating how these assessments are done to include more realistic earthquake behavior.

---

\*Corresponding author: [dmelgarm@uoregon.edu](mailto:dmelgarm@uoregon.edu)

# 1 Motivation

## 1.1 A brief overview of tsunami hazard assessments

Tsunamis, particularly those that result from earthquakes, continue to be a major hazard source for coastal communities. Between 1998 and 2017 they were responsible for 20% of all fatalities caused by natural hazards and 10% of all associated economic losses (UNDRR, 2018). These figures are profoundly influenced by the 2004 M9.2 Sumatra, Indonesia and the 2011 M9.0 Tohoku, Japan, earthquakes (Mori et al., 2011; Titov et al., 2005) which had far-reaching effects – these sobering numbers highlight the importance of developing quantitative methodologies for establishing the plausible tsunami intensities a particular region can expect in the future.

Assessments of tsunami hazards that attempt to quantify this typically fall into two categories: Deterministic scenarios, and fully probabilistic calculations, with the choice of approach depending on the application. The use of scenarios is common in emergency planning and community organization where a fully probabilistic calculation may be considered unnecessarily complex and potentially obfuscating the purpose of the hazard assessment. In this approach a large event, sometimes dubbed the *maximum credible tsunami*, is defined based on expert consensus, hydrodynamic modeling is carried out to establish amplitudes or inundation extents and the results are then used to create products suitable for the chosen application. The choice of event, and with what fidelity it captures what is actually likely, has a first-order impact on the usefulness of the hazard assessment when a tsunami finally occurs.

The second and more complex approach is a probabilistic tsunami hazard analysis (PTHA) – a review of the fundamentals of this framework can be found in Grezio et al. (2017). Generally, a suite of tsunami sources (earthquake or otherwise) are assumed and used as initial conditions for hydrodynamic propagation. Tsunami waves are modeled from the locations of the sources to the sites of interest. Importantly, rates of occurrence of each tsunami source or sources must be defined, and at this point, a mathematical formalism, first defined by Geist and Parsons (2006), can be used to calculate a *tsunami hazard curve* which reflects the probability of exceeding a certain tsunami amplitude over a certain period of time called the *return period*. By way of illustration, Figure 1 depicts an example hazard curve for the town of Sitka, Alaska, obtained from the results of this work, the particulars of the computation are explained later – it shows that, if the calculation is to be believed, there is a ~50% chance of a tsunami that exceeds (is larger) than 2 m in the next 50 years. This probability increases to ~80% if we instead consider the next 125 years and becomes a near certainty if we consider the next 500 years. These curves codify such probabilistic statements and are very useful because they allow engineers to select specific return periods relevant to the design of different kinds of structures. The tsunami flow depths at a specific probability level and return period, as well as other useful quantities like the flow speed, can be used by engineers as the *load* that a specific structure needs to be built to withstand. In the example in Figure 1 the 50 year return period might be a useful guide for design of single-family homes or residential apartments whose useful life might not be expected to exceed too much longer than that. However, for designing critical infrastructure a longer return period such as 500 years might be more suitable, and even, perhaps, not long enough.

PTHA has found significant success, and numerous research articles as well as technical documents from operational agencies exist which detail how the framework can be applied to specific contexts. These regions include Australia (Davies and Griffin, 2018), Chile (González et al., 2020), Indonesia (Sørensen et al., 2012), the Mediterranean

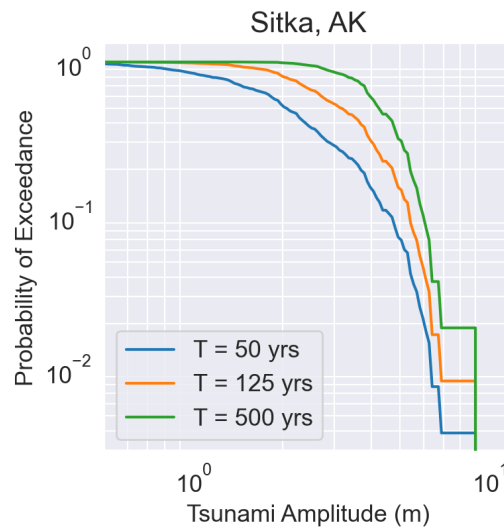


**Figure 1** Example tsunami hazard curves for Sitka, Alaska. Shown are curves for 3 return periods, 50, 125, and 500 years.

69 (Horspool et al., 2014), Mexico (Salazar-Monroy et al., 2021), the South China Sea (Li et al., 2016; Sepúlveda et al., 2019),  
 70 the United States (University of Washington Working Group, 2017), just to name a few. Of note is that, when a prob-  
 71 abilistic calculation for the tsunami hazard is made, we typically distinguish between *near-field* sources which are  
 72 close to the site of interest and *far-field* sources which are further afield, sometimes an entire ocean basin away. In  
 73 this paper I focus on the dominant source of hazard which are earthquake induced tsunamis and zero in on a poten-  
 74 tial characteristic of them that can affect a PTHA calculation: the details of the time-evolution – the kinematics – of  
 75 the rupture process.

## 76 **1.2 Rupture complexity: kinematics and tsunamigenesis**

77 There are numerous complexities associated with the rupture process which may contribute to the particularities of  
 78 tsunamigenesis and have been the subject of scrutiny in the literature before.

79 The most important one is perhaps the heterogeneity of slip. Out of a desire to minimize uncertainty and due to  
 80 the fact that future slip distributions of large events are, at present, impossible to forecast, tsunami hazard assess-  
 81 ments have relied on homogeneous or very simplified slip distributions (González et al., 2009; Witter et al., 2011).  
 82 More recently, there has been a concerted effort to use more realistic heterogeneous slip distributions (Geist and  
 83 Lynett, 2014; Davies et al., 2015; Mori et al., 2018) and in fact, Melgar et al. (2019) noted, through numerical exper-  
 84 imentation, that, all things being equal (fault length and width, depth, and magnitude) heterogeneous slip leads  
 85 to consistently larger tsunami amplitudes in the near-field of an earthquake compared to homogeneous or quasi-  
 86 homogeneous slip. The issue has been discussed for far-field modeling as well (Davies and Griffin, 2018) with the  
 87 same conclusion being reached – that simplified slip distributions bias tsunami calculations towards the low end of  
 88 the spectrum. A modern tsunami hazard assessment must consider realistic slip heterogeneity.

89 In these previous works, and many others, the issue of the time evolution of slip, the rupture kinematics, has  
 90 received some cursory attention. Typical rupture speeds for most tsunamigenic earthquakes are  $\sim 2.5\text{-}3.5$  km/s (Mel-  
 91 gar and Hayes, 2017), meanwhile tsunami propagation speeds in water depths of 100-1000m, typical of continental  
 92 shelves, are a much slower 0.03-0.1 km/s. From this rudimentary calculation alone, one would expect the kinematics  
 93 of rupture to have no measurable influence on the ensuing tsunami. The rupture propagates so fast, from the point

of view of the tsunami waves, that it is essentially instantaneous.

Because of this, it is common in tsunami modeling to assume that the deformation associated with an earthquake that sets up the tsunami initial condition occurs instantaneously (Grezio et al., 2017). This is attractive because it can speed up computation— capturing the full details of time-evolving crustal deformation and its coupled relationship to tsunamigenesis requires taking modeling time steps during the rupture process that are much shorter than what is required if instantaneous deformation can be assumed. Indeed, a numerical study by Williamson et al. (2019) found that in the near field there is less than a 1% difference in tsunami amplitudes resulting from considering instantaneous vs. time-dependent crustal deformation associated with the earthquake.

Two important corollaries to the above results are worth mentioning. First, when ruptures are very slow, close to the propagation speeds of tsunamis in continental shelves, then the effects can be significant and might lead to larger tsunamis than when considering instantaneous rupture (Riquelme et al., 2020; Riquelme and Fuentes, 2021). Slow earthquakes like this are very rare, however, and restricted to the special class labeled "tsunami earthquakes" which rupture the shallow-most part of a subduction zone and create tsunamis that are much larger than expected for their magnitude while also radiating very weak seismic energy (Satake, 1994; Newman and Okal, 1998; Hill et al., 2012; Sahakian et al., 2019). The second instance where rupture speed can play a significant role was identified by Williamson et al. (2019) and has to do with far-field tsunamis. There, the modeling showed that while the impacts in the near-field were negligible, in the far-field there was enough time, given the long propagation distances, for the differences to amount to meaningful variations in amplitude, especially for long, high magnitude, unilateral ruptures where the source process can take many minutes. That study simply mentioned this potential difference without analyzing it in detail as their focus was the near-field hazard. However, there exists some limited evidence that rupture kinematics, in fact, need to be considered in the far-field. Modeling open-ocean observations from the TOPEX/Poseidon satellite altimeter that measured the tsunami waves in the deep Indian Ocean from the extremely long rupture (~1600 km, ~10 min) associated with the 2004 M9.2 Sumatra earthquake appears to indeed require consideration of the time evolution of rupture (Fujii and Satake, 2007; Suppasri et al., 2010).

### 1.3 Hypothesis tested in this work

Given the context discussed above, in this work I expand on the findings of Williamson et al. (2019) and use numerical models to explore the impacts of rupture kinematics in *far-field* tsunamis. Specifically, I test the hypothesis that rupture can be safely assumed to be instantaneous. I will conclude that it cannot, and that ignoring rupture kinematics can have a measurable impact in estimated far-field tsunami amplitude that cannot be ignored. Finally, I discuss potential approaches for formally including rupture kinematics in hazard assessments.

## 2 Methods

In order to focus specifically on the issue of rupture kinematics, and because they were studying primarily near-field effects Williamson et al. (2019) created a sandbox subduction zone with simplified bathymetry and with infinite length along-strike. That approach was valuable, it allowed the authors to untangle confounding variables such as the complexity introduced by bathymetry. Here, I focus on far-field effects where it is harder to create a useful simplified spherical model of the world's oceans. Instead, I selected a ~1,500 km segment of the Alaskan subduction zone (ASZ,



130 Figure 2) as the source region. I place different homogeneous sources there and propagate the tsunamis to far-field  
 131 virtual tide gauges to study the impacts of different source kinematics.

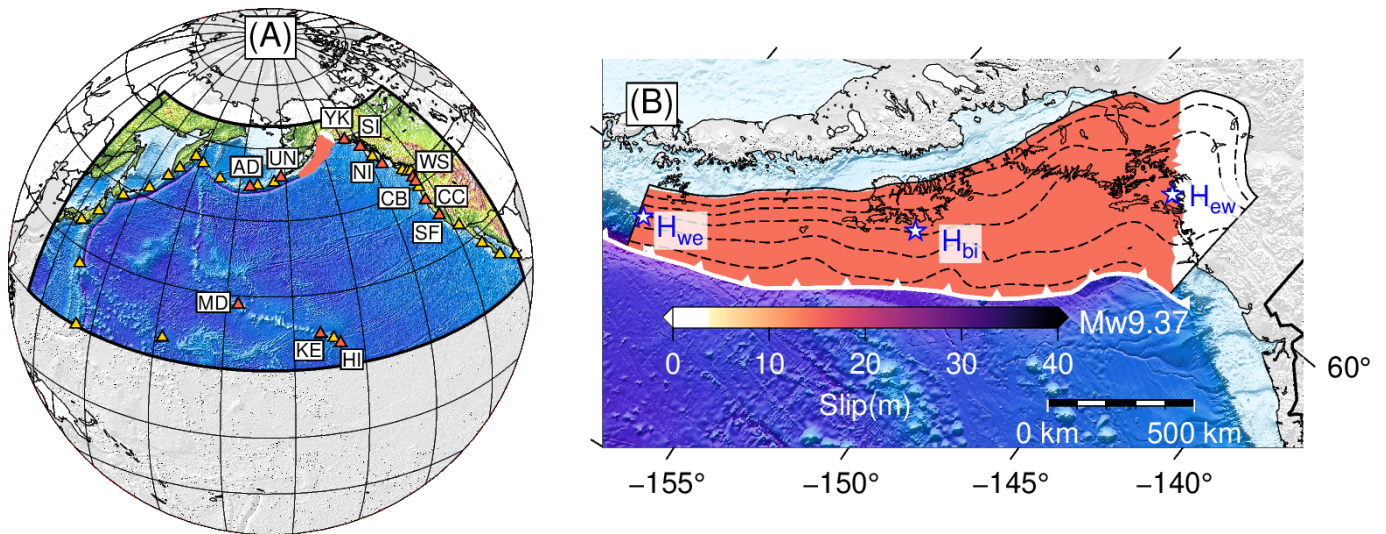


**Figure 2** (A) Domain used for hydrodynamic propagation modeling. The portion of the Alaskan subduction zone assumed as the source region is shown in pink. Triangles are the virtual tide gauge stations used to collect model output. Stations mentioned elsewhere in the article are AD-Adak, UN-Unalaska, YK-Yakutat, SI-Sitka, NI-Ninstints, WS-Westport, CB-Cannon beach, CC-Crescent City, SF-San Francisco, HI-Hilo, KE-Kealia, and MD-Midway. (B) Close-up of the approximately 1500 km long stretch of the Alaskan subduction zone used as a source region in this study. Shown is a homogeneous slip M9.37 earthquake. Slab geometry is from Slab 2.0 (Hayes et al., 2018) and contoured every 10 km in depth. Three possible hypocenter to nucleate rupture are shown,  $H_{we}$  for unilateral west to east rupture,  $H_{bi}$  for bilateral rupture, and  $H_{ew}$  for unilateral east to west rupture.

## 132 2.1 The earthquake sources assumed and their kinematics

133 As noted previously, slip heterogeneity can have significant impacts on the details of a tsunami. Here, however, to  
 134 focus on the contributions of kinematics, I rely primarily on homogeneous slip. In the discussion I will touch on the  
 135 added contributions of heterogeneous slip with a single example.

136 I chose the segment of the ASZ shown in Figure 2B primarily because it is large enough to fit earthquakes as large as  
 137 the 1964 M9.2 event (Ichinose et al., 2007) and can thus be assumed to reasonably represent a source region capable of  
 138 hosting hazardous events across a broad range of magnitudes. I then created homogeneous slip sources spanning the  
 139 magnitude range M7-M9.5 using 0.1 magnitude unit bins and 100 events per bin for a total of 2600 ruptures. Because it  
 140 is well established that for a given magnitude earthquakes can have different dimensions (Blaser et al., 2010; Allen and  
 141 Hayes, 2017) the ruptures are allowed to vary in their length and width. For each earthquake I make a random draw  
 142 from the probabilistic length and width scaling laws for thrust earthquakes from Blaser et al. (2010). I then select a  
 143 random segment of the megathrust region in Figure 2B and then compute how much homogeneous slip is necessary  
 144 to reach the target magnitude. For the fault geometry I use the 3D slab model of (Hayes et al., 2018), discretize it into  
 145 triangular subfaults, and allow slip from the trench to a maximum seismogenic depth of 60 km which is consistent  
 146 with the 1964 M9.2 earthquake (Ichinose et al., 2007) and also with the more modestly sized and more recent 2020  
 147 M7.8 and 2021 M8.2 Simeonof and Chignik earthquakes (Crowell and Melgar, 2020; Ye et al., 2022). A summary of the  
 148 rupture dimensions is shown in Figure 3 and an example of a homogeneous slip source that results from this process  
 149 is in Figure 2B. Finally for the Earth structure I assume a homogeneous half-space with rigidity of 30 GPa.

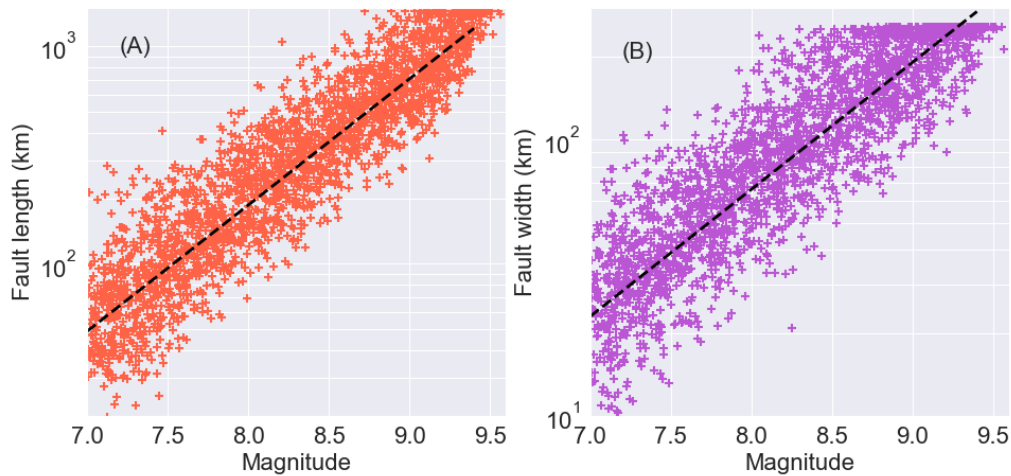


**Figure 3** (A) Rupture length vs. magnitude scaling. The symbols are the length of each rupture and the dashed line is the median expected length from [Blaser et al. \(2010\)](#) (B) Rupture width vs. magnitude scaling. The symbols are the length of each rupture and the dashed line is the median expected length from [Blaser et al. \(2010\)](#)

150 In terms of kinematics I assume a standard uniform rupture speed of 3.0 km/s consistent with worldwide observa-  
 151 tions of megathrust ruptures ([Melgar and Hayes, 2017](#)). For each rupture a hypocenter is chosen at random from all  
 152 the subfaults that participate in a particular event and the inter-fault distance is calculated based on a spline interpo-  
 153 lation on the assumed 3D fault surface. The "onset time", which is the time after the event origin at which the rupture  
 154 from the hypocenter reaches a sub-fault is then simply the inter-fault distance divided by the assumed rupture speed.  
 155 An example of the impact this can have on rupture duration is shown in [Figure 4](#) where I have forced the hypocenter  
 156 to be at either edge of an almost full margin M9.3 earthquake representing purely unilateral rupture. Shown as well  
 157 is an event where rupture initiates in the middle for a purely bilateral earthquake. In the full-suite of events shown  
 158 in [Figure 3](#) because the hypocenter is assigned at random there is a mix of kinematic behaviors between these two  
 159 extremes.

## 160 2.2 Hydrodynamic modeling

161 I employed the GeoClaw modeling framework ([Berger et al., 2011](#)), an open-source module within the Conservation  
 162 Laws Package (Clawpack) suite ([Mandli et al., 2016](#); [Clawpack Development Team, 2024b](#)), to simulate tsunami gen-  
 163 eration, propagation, and inundation. The tsunami initial condition is the seafloor deformation produced by each  
 164 earthquake. For both instantaneous or static, and kinematic ruptures I calculate the crustal deformation using the  
 165 triangular subfault approximation to the analytical solutions of [Okada \(1985, 1992\)](#) as implemented in GeoClaw. The  
 166 code then solves the depth-averaged shallow water equations using high-resolution finite volume methods, making it  
 167 well-suited for capturing the nonlinear dynamics of tsunami waves and their interaction with complex coastal topog-  
 168 raphy. To ensure numerical stability and accuracy, I set the Courant-Friedrichs-Lewy (CFL) condition to 0.75, limiting  
 169 the time step size relative to the spatial grid size and wave speed. GeoClaw can handle wetting and drying processes,  
 170 allowing for accurate simulation of onshore wave run-up and inundation. Tsunami waves are propagated over vari-  
 171 able bathymetry and topography, I used the ETOPO2 2 arcmin bathymetry dataset ([NOAA, 2006](#)) in deep water and the  
 172 30 arcsec SRTM30+ dataset in coastal regions ([Becker et al., 2009](#)). GeoClaw incorporates adaptive mesh refinement  
 173 (AMR), which dynamically increases computational resolution in regions of interest, such as near the tsunami source

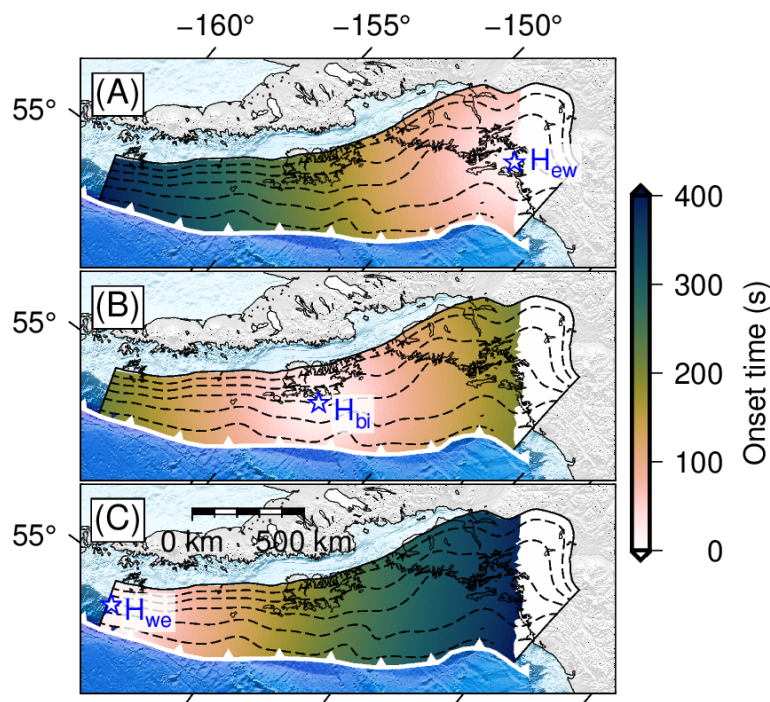


**Figure 4** (A) Rupture onset times for a unilateral east-west propagating homogeneous slip M9.3 rupture. (B) Same as in (A) but for a bilaterally propagating rupture. (C) Same as in (A) but for a unilateral west-east propagating rupture

174 or along the inundation zones, while maintaining efficiency in open-ocean areas. I used 3 AMR levels, the coarsest  
 175 grid has 10 arcmin resolution, the intermediate grid 2 arcmin to match the ETOPO2 data, and the finest grid 30 arcsec  
 176 to match SRTM30+. The model domain (Figure 2) covers 145° in longitude from 120° to 265° and 60° in latitude from  
 177 10°N to 70°N. Each tsunami model was run for a propagation time of 14 hours. GeoClaw has been rigorously validated  
 178 against laboratory experiments and historical tsunami events, ensuring its reliability for hazard assessment and risk  
 179 analysis (González et al., 2011; Arcos and LeVeque, 2015).

### 180 **3 Results and Discussion**

#### 181 **3.1 Slip kinematics rotate the far-field tsunami radiation pattern**

182 The most immediate result from the hydrodynamic modeling is to confirm what Williamson et al. (2019) had already  
 183 identified – rupture directivity rotates the tsunami radiation pattern. In Figure 5 I show the maximum tsunami am-  
 184 plitude from assuming an instantaneous rupture, a bilateral one, an east to west one, and another west to east rupture  
 185 for the same M9.3 homogenous slip distribution shown in Figures 2B,4 . To first order what can be seen is that the  
 186 tsunami *roughly* increases in amplitude in the direction of rupture, for example for East to West rupture the tsunami  
 187 is larger in Hawaii which is due West of the the subduction zone and smaller when the rupture is West to East. For  
 188 a bilateral rupture the pattern is a combination of these effects. The effect can be significant, Figure 6 shows the  
 189 differences at Hilo, Hawaii, of the tsunami when rupture is assumed instantaneous versus when it has unilateral di-  
 190 rectivity. When rupture is "towards" Hilo (east to west) the tsunami is about 1 m larger by peak amplitude for the first  
 191 4 arriving waves. Likewise when the rupture is "away" from Hilo in the west to east direction the tsunami is slightly  
 192 smaller than in the instantaneous case but also decays much faster. Interestingly the coda of the tsunami (after about  
 193 3 hours) has very similar amplitudes in all cases.



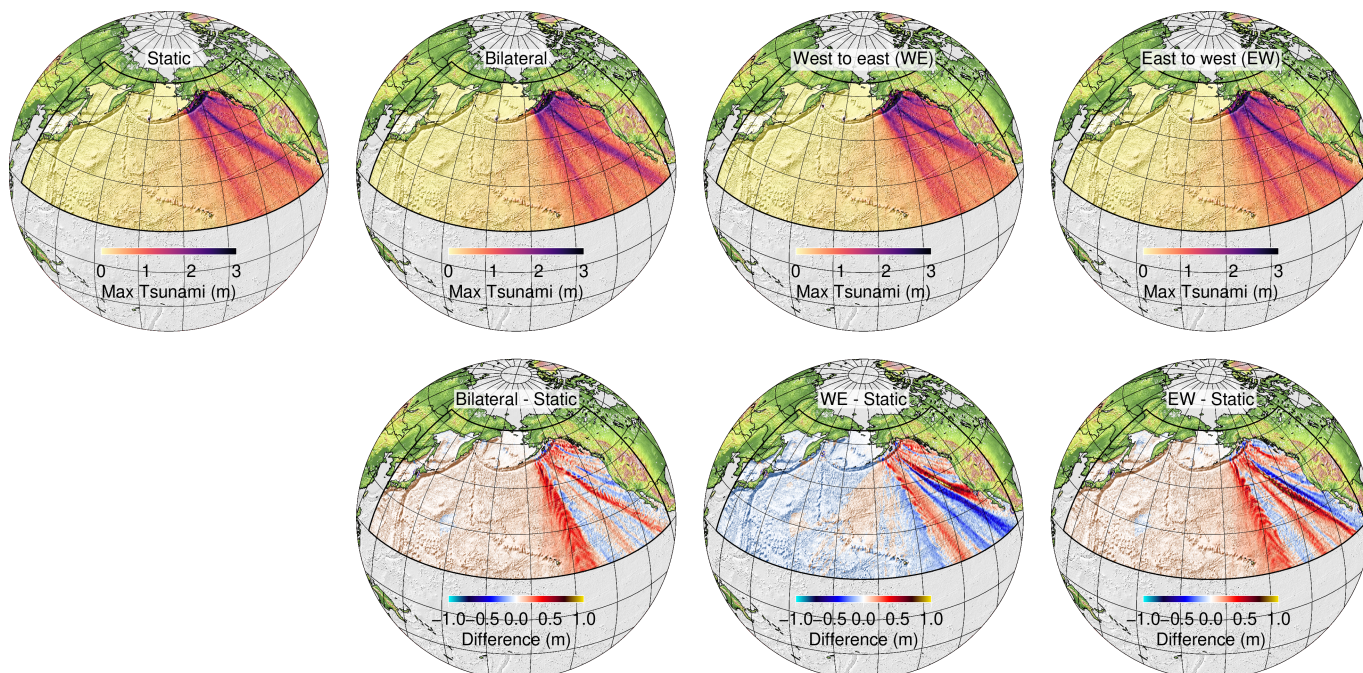


**Figure 5** Maximum tsunami amplitudes resulting from assuming an instantaneous (static) rupture vs. unilateral east to west, west to east, or bilateral ruptures shown in Fig. 4 Differences between the time-dependent kinematic ruptures and the static one are shown as well.

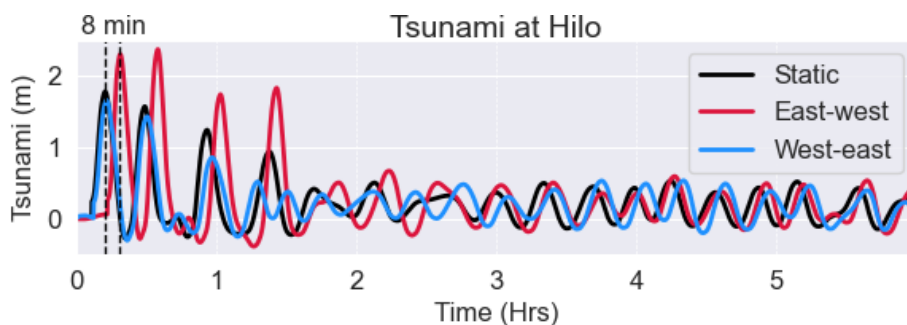


**Figure 6** Tsunami amplitude at Hilo, Hawaii from instantaneous (static) rupture of the earthquake shown in Figure 2 and from time-dependent rupture with east to west or west to east directivity. Note the 8 min arrival time difference for the peak amplitude

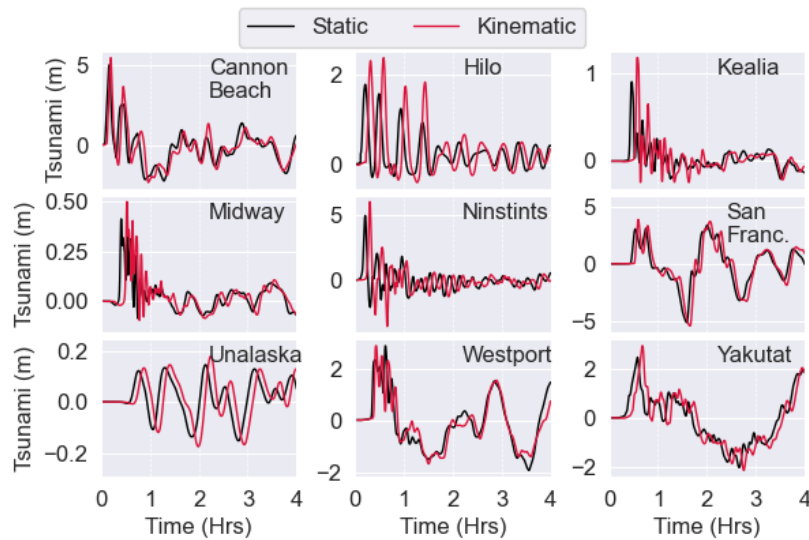


**Figure 7** Comparison of tsunami amplitude at at selected sites between instantaneous or static rupture and unilateral "kinematic" rupture. For some fo the sites the maximum difference is with the east to west rupture, for others with the west to east rupture.

194 Figure 7 shows the effect at other sites across the basin. For each one I selected a kinematic rupture that shows  
 195 some amplitude difference with respect to the instantaneous rupture assumption, sometimes that is the east to west,  
 196 others the west to east. I highlight, however, that tsunami propagation is non-linear and bathymetry complex so the  
 197 effect isn't that simple or easy to anticipate before the modeling is run. Depending on the complex interplay between  
 198 those two factors, for any given rupture the resulting tsunami can be smaller or larger at a specific site. This is shown  
 199 in Figure 8 where I plot the relative and absolute differences in maximum amplitudes between the instantaneous and  
 200 different kinematic ruptures at a variety of coastal sites. Overall there is a trend where if rupture is towards a site the  
 201 amplitude is larger than if it is away from it. The bilateral rupture is a complex combination of both and there are  
 202 numerous sites which for the event plotted are exceptions to this trend.

203 Evidently the effect is a strong function of source duration which itself is a function of magnitude – larger events  
 204 rupture longer faults and have longer source processes with more time for the kinematic effect to be manifest. Figure  
 205 9 shows an example of this. Here, I have plotted the differences between instantaneous and kinematic ruptures for  
 206 events with M7.8, M8.3, and M8.8 and can be compared and contrasted with the effect for an M9.3 rupture in Fig.  
 207 8. The differences are more and more significant with increasing magnitude, they are smaller than 5% for the M7.8  
 208 event and as large as 30% for the M9.3 event. Now, while these changes are most important for the largest events,  
 209 even for more "modest" ruptures like the M8.3 shown in Fig. 9 the differences can be as high as ~10-15% suggesting  
 210 that, when considering ensembles of ruptures, such as in PTHA, the effect might have a measurable impact in the  
 211 resulting hazard calculation, this will be discussed at length soon.

### 212 3.2 Implications for single event hazards assessments

213 The purpose of selecting a MCE, whether for far- or near-field sources, is to have a single scenario from which prod-  
 214 ucts such as inundation maps or evacuation times can be produced, and which reflects a credible worst case. The  
 215 goal is to avoid the complexities and potential confusion of a full probabilistic calculation while at the same time  
 216 producing information that reflects what is possible and is actionable and useful.

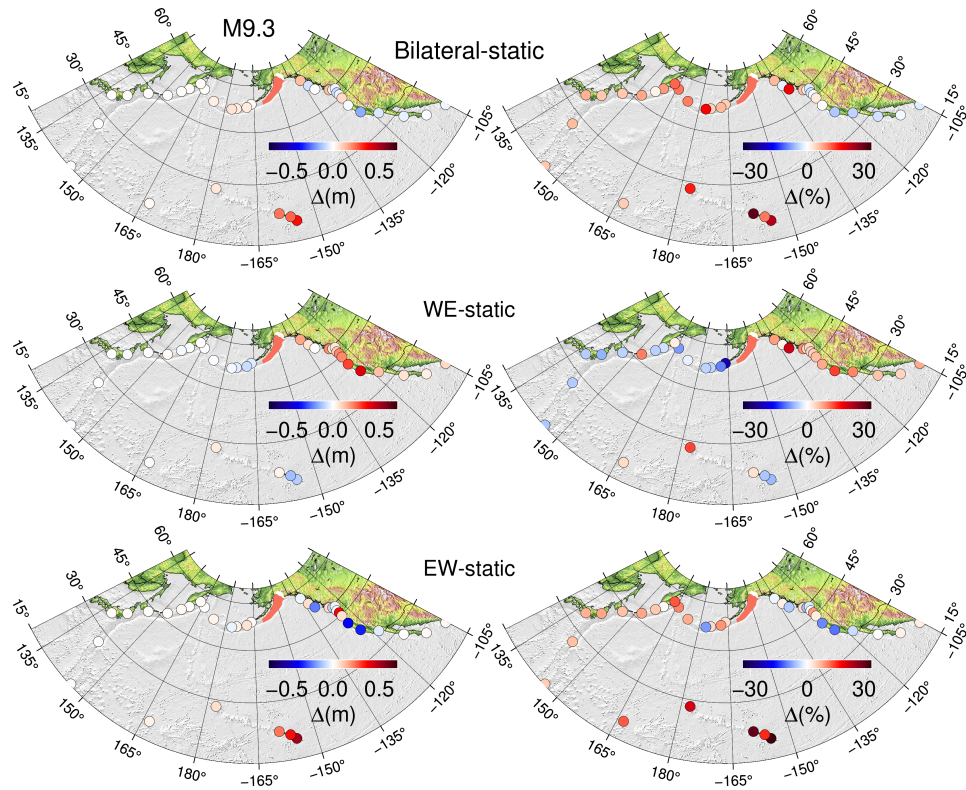


**Figure 8** Differences in the maximum recorded amplitudes at coastal sites between instantaneous (static) rupture, and bilateral, and east to west (EW), or west to east (WE) rupture. The differences are shown as absolute values (left column) and relative percentages (right column)

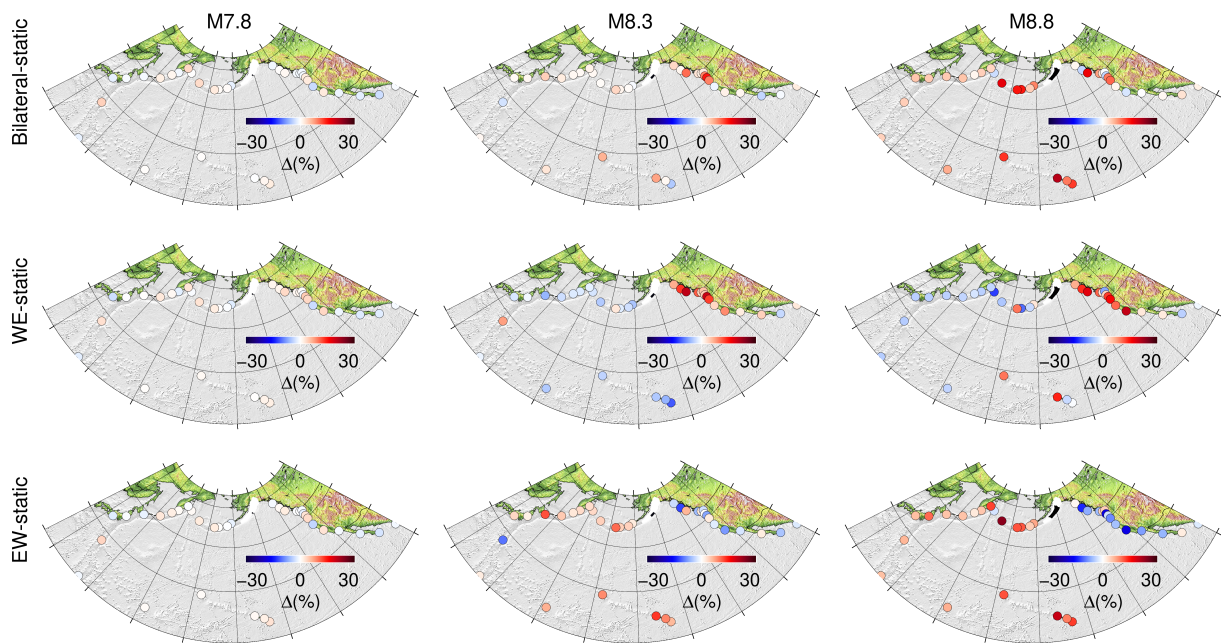


**Figure 9** Differences in the maximum relative recorded amplitudes at coastal sites between instantaneous (static) rupture, and bilateral, east to west (EW), or west to east (WE) rupture for homogeneous slip models with M7.8, M8.3 and M8.8.



As an example of this, for both Hawaii and the western states of Washington, Oregon, and California, events in Alaska are considered the dominant source of far-field hazard and simple quasi-homogeneous slip single scenarios routinely used for hydrodynamic calculations and product generation (González et al., 2009; Priest et al., 2013; Butler et al., 2017). Figure 10 reflects the potential impacts of considering more realistic sources. I produced a stochastic heterogeneous M9.3 slip model (Figure 10A) covering the exact same extent as the homogeneous slip model in Figs. 2B,4 and calculated the resulting tsunami, both when assuming an instantaneous rupture process, and when assuming a completely unilateral east to west rupture. The tsunami time series at the same locations as in Figure 8 are shown in Figure 10B. The differences can be significant when moving from a homogeneous instantaneous rupture to a heterogeneous instantaneous rupture. At Hilo, HI, where we already knew the effect would be important, the peak amplitudes increase by 39% between the homogeneous static and heterogeneous static sources and by 86% between the homogeneous static and heterogeneous kinematic. At other U.S. west coast sites like Westport, WA, Cannon Beach, OR and San Francisco, CA, the effect is more modest, closer to a ~10-20% increase. Notably considering a kinematic heterogeneous slip rupture increases the amplitudes, not just of the first arrivals, but frequently of the entire wavetrain.

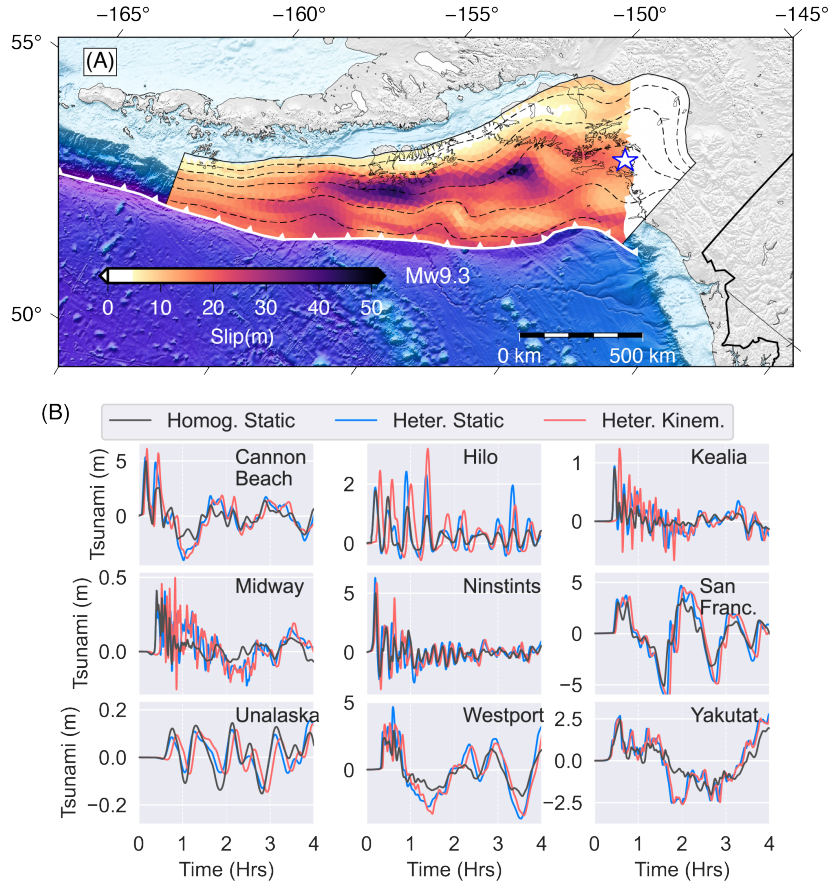
Overall, what can be observed in Figure 10 is that allowing for more realistic heterogeneous slip has a major impact, this has been clearly articulated already by Davies and Griffin (2018) and Melgar et al. (2019), but compounding that increase, the source kinematics could potentially make an already impactful event significantly worse. The conclusion here is that modelers and hazards practitioners, when ideating MCEs, should consider potential tsunami directivity from source kinematics.

### 3.3 Consideration of kinematics can increase hazard in far-field PTHA calculations

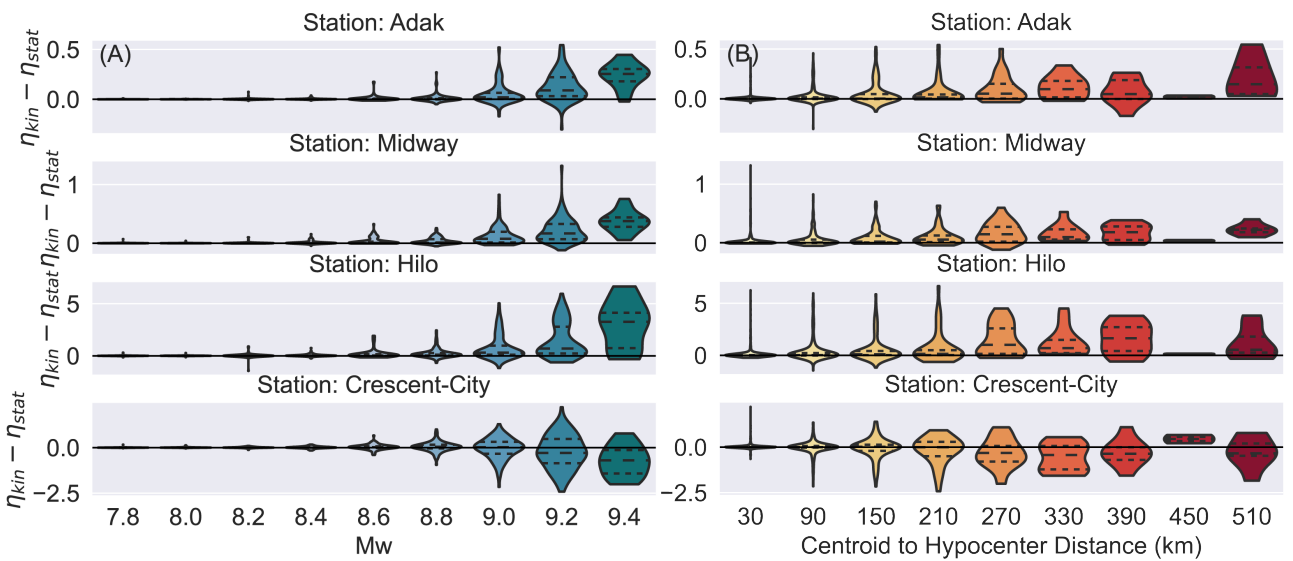
Figures 8-10 tell a compelling narrative that the source kinematics can matter in the far-field and can frequently make peak amplitudes appreciably higher. But they also show that kinematics can *sometimes* make the amplitudes smaller. So, for applications such as PTHA, where we consider ensembles of ruptures, an obvious question is whether source kinematics increase, decrease or leave the overall hazard unchanged when compared to the instantaneous rupture assumption. This will ultimately dictate how modelers should consider this increased source complexity in formal PTHA calculations.

Figure 11A shows a summary of the differences for all 2600 ruptures at four selected sites which are representative of the overall behaviors seen across the basin. At three of them (Adak, Midway, and Hilo) the effect is to increase the overall hazard – this is more clearly visible as the magnitude increases. This can also be readily seen in Figure 11B as a function of the distance between the centroid and the hypocenter, which is a proxy of how unilateral a rupture is. The effect is noticeable for distances as short as 90-150 km and is extremely prominent for the longer distances. For one of the sites (Crescent City) the effect is sometimes to increase the amplitude, both as a function of magnitude and centroid-hypocenter distance, but other times the amplitude is decreased. At that site in particular we see that the median differences are negative – kinematics reduce the overall hazard.

What is the impact of this on a fully probabilistic hazard calculation? For each coastal site I calculated the hazard curves using the PTHA formulation described in Melgar et al. (2019). For the magnitude frequency distributions (MFDs) I assumed a linear Gutenberg-Richter-like distribution and a tapered one that has decreasing rates for all



**Figure 10** Effect of slip kinematics on single scenario tsunami hazard estimates. (A) Heterogeneous stochastic slip M9.3 covering the same rupture are as the event in Figs.2,4. The blue star is the hypocenter. (B) Resulting tsunamis at Hilo, HI.



**Figure 11** Differences between peak tsunami amplitude from kinematic sources ( $\eta_{kin}$ ) and from static or instantaneous rupture ( $\eta_{stat}$ ) for all events at four selected sites (A) Results disaggregated into magnitude bins and (B) into distance between the rupture centroid and the hypocenter. For each violin the median and quartiles are shown in dashed lines.

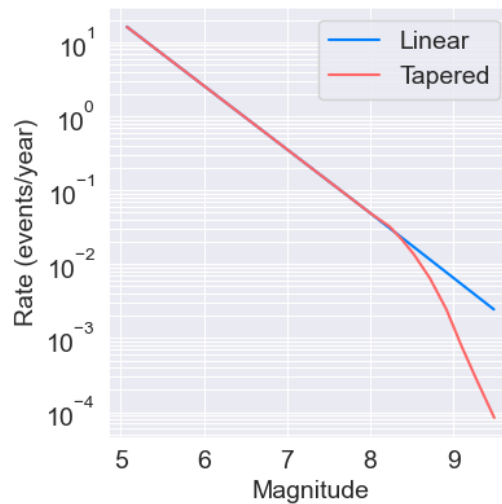


**Figure 12** Magnitude frequency distributions assumed for hazard curve calculations taken from Powers et al. (2024)

254 events with  $M_w > 8.3$ . The distributions are shown in Figure 12 and both are taken from the U.S. National Seismic  
 255 Hazard Map for Alaska as described by Powers et al. (2024). The resulting hazard curves for the same four sites  
 256 as Figure 11 are shown in Figure 13. For the same three sites where we saw significant amplitude increases (Adak,  
 257 Midway, and Hilo) when considering kinematic ruptures we see significant increases in the resulting hazard curves.  
 258 Because the amplitude differences are greatest at larger magnitudes and these events have lower rates of occurrence,  
 259 I had hypothesized that this effect would be much more pronounced at long return intervals such as  $T = 500$  yrs.  
 260 However, the increase in hazard is evident for the much shorter return period of  $T = 50$  yrs as well. This is most likely  
 261 a result of the fact that the increase to hazard due to source kinematics is non-negligible for events with "modest"  
 262 magnitudes as well as for those with relatively short centroid-hypocenter distances (Figure 11).

263 For Crescent City, where the kinematic ruptures frequently produced smaller amplitudes than the static ones  
 264 (Figure 11) I do indeed find a very slight reduction in hazard when considering the kinematic source process. As  
 265 interesting as this behavior is, it is not the norm, only at 5 of the coastal sites is there a slight reduction in hazard  
 266 while at the rest the hazard increases when considering kinematic ruptures.

267 I note that another important factor to consider is the overall impact that kinematic ruptures might have on the  
 268 resulting hazard curves when considering different MFDs. The tapered distribution shown in Figure 12 has a much  
 269 lower yearly rate of occurrence for large events. A priori, one might think this would make the effect of considering  
 270 kinematic sources less significant because those events where the difference is largest receive a smaller weight in the  
 271 calculation. However, in Figure 14 I show the hazard curves for the tapered distribution compared to the log-linear  
 272 Gutenberg-Richter distribution and find that this is not the case. Overall, yes, the tapered MFD leads to a substantially  
 273 lower hazard compared to the linear MFD, because large vents are occurring less frequently, but for any given MFD,  
 274 the difference between static and kinematic sources remains. This suggests strongly that, even with an MFD that  
 275 reduces the frequency of large events, considering kinematics remains important.

### 276 **3.4 Limitations of the approach, other confounding variables, and open questions**

277 Finally, I note a few limitations of the approach and confounding variables that can affect my interpretation of the  
 278 impact of source kinematics on far-field tsunami hazard assessments.

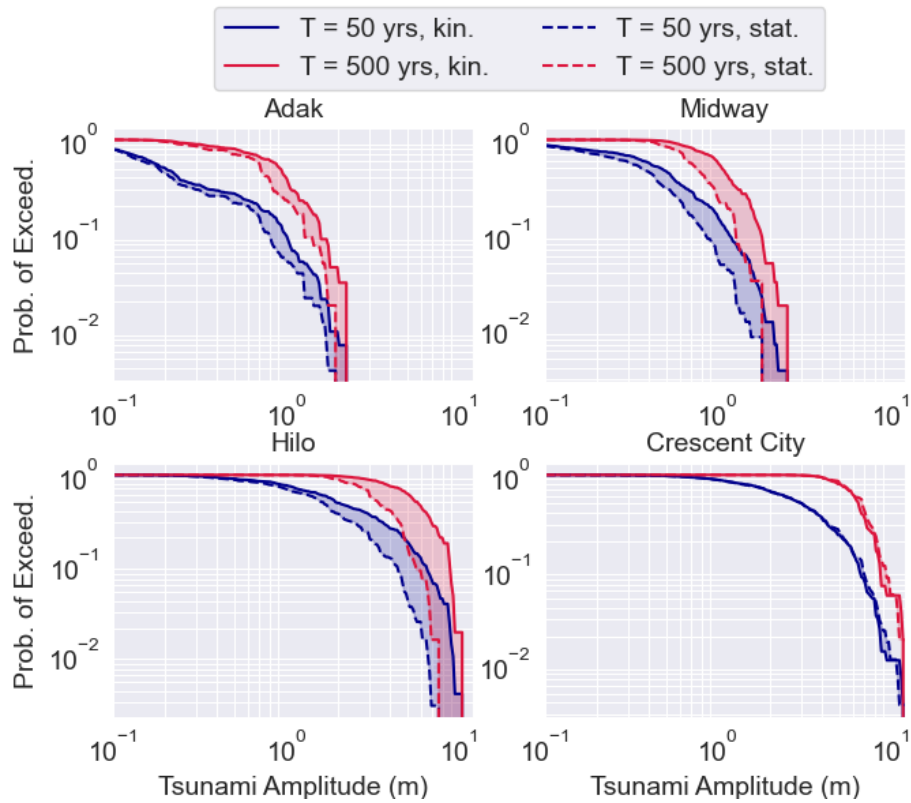


**Figure 13** Hazard curves at two return periods ( $T = 50, 500$  yrs) for the same four coastal sites as Figure 11. The curves assuming instantaneous sources are shown in dashed lines and the ones for kinematic ruptures are in solid lines. The difference between them are shaded for clarity

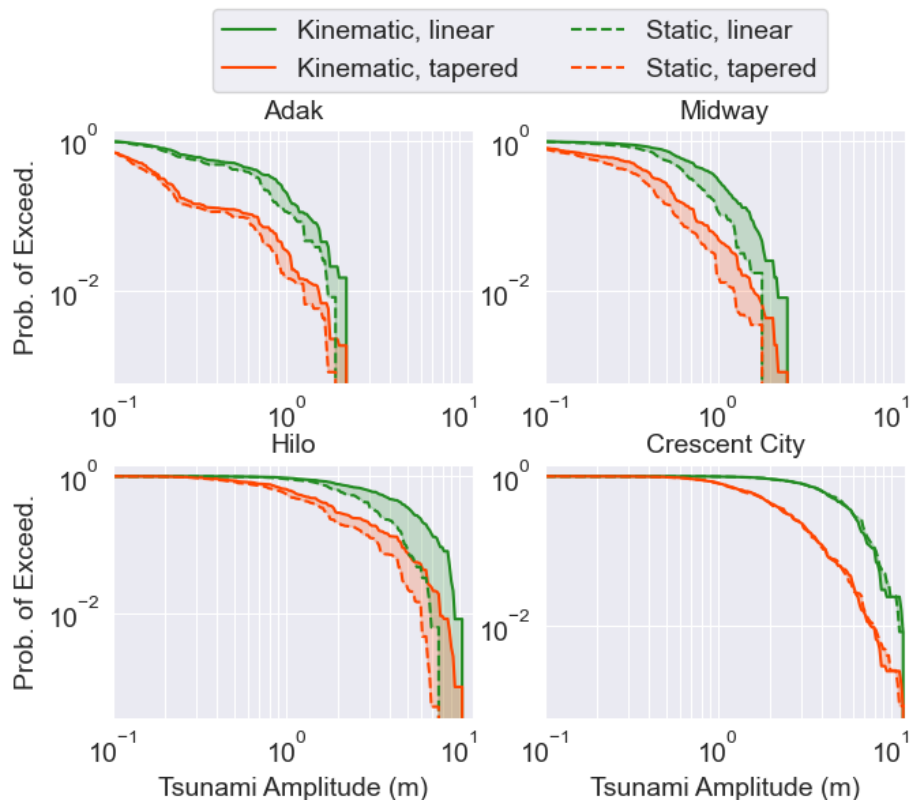


**Figure 14** Hazard curves at a return period of  $T = 125$  yrs assuming the two magnitude frequency distributions (linear and tapered) from Figure 12 and the impact between static and kinematic ruptures. The difference between them are shaded for clarity

279 The hydrodynamic code I used does not account for dispersion. Studies have shown that, particularly in the  
280 far-field, dispersion can significantly alter arrival times and, due to non-linear propagation, the way that different  
281 phases of the tsunami wave train interact with each other (Glimsdal et al., 2013; Grilli et al., 2013; Baba et al., 2017).  
282 This means that, if modeling of time series at trans-oceanic distances requires very accurate interactions between  
283 phases then dispersion cannot be ignored. However, in those previous works significant impacts to peak amplitudes  
284 have not been observed. So, while dispersion would likely change some of the details of the shapes of the time series  
285 seen in Figures 6,7 and 10 I would not expect the general finding– that source kinematics have a meaningful impact  
286 on far-field tsunami hazards, to change. Nonetheless, I recognize that an accurate PTHA calculation that seeks to be  
287 useful for decision-making products ought to account for this added complexity.

288 Bathymetry remains an important confounding variable and one whose impact is difficult to ascertain before the  
289 modeling is carried out. Due to the complexity introduced by non-linear tsunami wave propagation it is possible for  
290 sites close to each other to be affected by the increased hazard introduced by kinematic sources to different degrees  
291 (e.g. Figures 8 ,9). So much so that, even if for the most parts we expect hazard will increase, some sites (such as  
292 Crescent City in this work) might see a slight reduction in hazard.

293 Of course, whatever the impact, the hazard curves in Figures 13,14 suggest that it is significant and it ought to be  
294 considered. I note, however, that the overall change to a specific site's hazard will be the sum of the far-field hazard  
295 contributions of many subduction zones, not jsut one, in addition to the contributions from any local sources. I stress  
296 that the findings here suggest that the tsunami hazard to, for example, Hilo is higher for events from Alaska, but it  
297 is not easy to see without further modeling whether this will be equally true for all far-field sources that affect that  
298 site and whether in aggregate this will lead to an overall more dangerous hazard curve. At most what I can say is that  
299 there is a significant chance that the present methodology used to infer far-field hazards is most likely systematically  
300 biased towards underestimating them, but quantifying to what extent this bias exists requires a significant amount  
301 of new numerical modeling.

302 Furthermore, the results shown here only account for impacts to coastal amplitudes and say nothing of how this  
303 potential increase in hazard will change inundation estimates. It is ultimately this inland extent and intensity of  
304 flooding that is of use for many applications such as evacuation maps. Because the increases in amplitudes extend  
305 to more than just the first or largest arriving wave (e.g. Figure 7) it is reasonable to expect that the impact will be  
306 non-negligible. I admit however, that that is speculation and highlight again that it is not easy to foretell the extent  
307 of the effect without new numerical modeling. With this in mind, and as a closing note to numerical modelers, I  
308 do in fact find that accounting for source kinematics slows down computation time – kinematic runs, depending on  
309 magnitude, are as much as 30% slower by CPU wall time. I argue here that this increased computational load is, in the  
310 face of the findings in this paper, an insufficient argument to justify ignoring an important effect. A modern far-field  
311 tsunami hazard assessment must account for source kinematics.

## 312 **4 Conclusions**

313 This study demonstrates that the commonly held assumption of instantaneous earthquake rupture in far-field tsunami  
314 modeling is not always valid. Using thousands of synthetic earthquake scenarios along the Alaskan subduction zone,

I show that rupture kinematics—particularly rupture direction and duration—can significantly alter the amplitude and arrival time of tsunami waves at distant coastlines.

Key findings include:

- Rupture directivity rotates the tsunami radiation pattern, increasing amplitudes in the direction of rupture and decreasing them in the opposite direction. This effect is amplified for larger earthquakes with longer rupture durations.
- Far-field sites, such as those in Hawaii and along the U.S. West Coast, can experience meaningful increases in tsunami amplitude—often exceeding 30%—when rupture kinematics are considered.
- Probabilistic tsunami hazard analysis (PTHA) incorporating rupture kinematics shows a consistent increase in hazard at most coastal sites, particularly for longer return periods and larger magnitudes. In rare cases, hazard can be slightly reduced, but this is the exception rather than the rule.
- The inclusion of rupture kinematics in deterministic scenario modeling (e.g., maximum credible events) can result in significantly different and potentially more realistic hazard assessments compared to traditional static assumptions.

These results imply that current far-field tsunami hazard assessments, which largely neglect source kinematics, are likely biased toward underestimating tsunami amplitudes. A general recommendation is that future PTHA frameworks and deterministic scenario development formally incorporate rupture kinematics to better reflect the physical processes that govern tsunamigenesis and to improve the reliability of hazard products used in coastal planning and infrastructure design.

## Data and code availability

Hydrodynamic modeling was carried out with the GeoClaw module of Clawpack v5.11, an open source code for solving the tsunami shallow water equations archived in Zenodo ([Clawpack Development Team, 2024a](#)). The stochastic source used in Figure 10 was generated using FakeQuakes, a module of MudPy open source stochastic rupture generator archived on Zenodo at [Melgar et al. \(2021\)](#). Ruptures used as input and hydrodynamic model output are also archived on Zenodo at [Melgar \(2025\)](#).

## Competing interests

The author declares no competing interest

## Acknowledgments

This work was partially funded by NSF Cooperative Agreement # 2225286. The research is also supported by NASA award #80NSSC23K1326.



## References

- 345
- 346 Allen, T. I. and Hayes, G. P. Alternative rupture-scaling relationships for subduction interface and other offshore environments. *Bulletin of*  
347 *the Seismological Society of America*, 107(3):1240–1253, 2017.
- 348 Arcos, M. E. M. and LeVeque, R. J. Validating velocities in the GeoClaw tsunami model using observations near Hawaii from the 2011 Tohoku  
349 tsunami. *Pure and Applied Geophysics*, 172:849–867, 2015.
- 350 Baba, T., Allgeyer, S., Hossen, J., Cummins, P. R., Tsushima, H., Imai, K., Yamashita, K., and Kato, T. Accurate numerical simulation of the  
351 far-field tsunami caused by the 2011 Tohoku earthquake, including the effects of Boussinesq dispersion, seawater density stratification,  
352 elastic loading, and gravitational potential change. *Ocean Modelling*, 111:46–54, 2017.
- 353 Becker, J., Sandwell, D., Smith, W., Braud, J., Binder, B., Depner, J., Fabre, D., Factor, J., Ingalls, S., Kim, S., et al. Global bathymetry and  
354 elevation data at 30 arc seconds resolution: SRTM30\_PLUS. *Marine Geodesy*, 32(4):355–371, 2009.
- 355 Berger, M. J., George, D. L., LeVeque, R. J., and Mandli, K. T. The GeoClaw software for depth-averaged flows with adaptive refinement. *Adv.*  
356 *Water Res.*, 34:1195–1206, 2011.
- 357 Blaser, L., Krüger, F., Ohrnberger, M., and Scherbaum, F. Scaling relations of earthquake source parameter estimates with special focus on  
358 subduction environment. *Bulletin of the Seismological Society of America*, 100(6):2914–2926, 2010.
- 359 Butler, R., Walsh, D., and Richards, K. Extreme tsunami inundation in Hawai‘i from Aleutian–Alaska subduction zone earthquakes. *Natural*  
360 *Hazards*, 85(3):1591–1619, 2017.
- 361 Clawpack Development Team. Clawpack v5.11.0, 2024a.
- 362 Clawpack Development Team. Clawpack software, 2024b. <http://www.clawpack.org>. doi: <https://doi.org/10.5281/zenodo.13376470>. Ver-  
363 sion 5.11.0.
- 364 Crowell, B. W. and Melgar, D. Slipping the Shumagin gap: A kinematic coseismic and early afterslip model of the Mw 7.8 Simeonof Island,  
365 Alaska, earthquake. *Geophysical Research Letters*, 47(19):e2020GL090308, 2020.
- 366 Davies, G. and Griffin, J. The 2018 Australian probabilistic tsunami hazard assessment: hazard from earthquake generated tsunamis. Tech-  
367 nical report, Geoscience Australia, 2018.
- 368 Davies, G., Horspool, N., and Miller, V. Tsunami inundation from heterogeneous earthquake slip distributions: Evaluation of synthetic source  
369 models. *Journal of Geophysical Research: Solid Earth*, 120(9):6431–6451, 2015.
- 370 Fujii, Y. and Satake, K. Tsunami source of the 2004 Sumatra–Andaman earthquake inferred from tide gauge and satellite data. *Bulletin of*  
371 *the Seismological Society of America*, 97(1A):S192–S207, 2007.
- 372 Geist, E. L. and Lynett, P. J. Source processes for the probabilistic assessment of tsunami hazards. *Oceanography*, 27(2):86–93, 2014.
- 373 Geist, E. L. and Parsons, T. Probabilistic analysis of tsunami hazards. *Natural Hazards*, 37:277–314, 2006.
- 374 Glimsdal, S., Pedersen, G. K., Harbitz, C. B., and Løvholt, F. Dispersion of tsunamis: does it really matter? *Natural hazards and earth system*  
375 *sciences*, 13(6):1507–1526, 2013.
- 376 González, F., Geist, E. L., Jaffe, B., Kânoğlu, U., Mofjeld, H., Synolakis, C., Titov, V. V., Arcas, D., Bellomo, D., Carlton, D., et al. Probabilistic  
377 tsunami hazard assessment at seaside, Oregon, for near-and far-field seismic sources. *Journal of Geophysical Research: Oceans*, 114  
378 (C11), 2009.
- 379 González, F. I., LeVeque, R. J., Chamberlain, P., Hirai, B., Varkovitzky, J., and George, D. L. Validation of the GeoClaw model. In *NTHMP MMS*  
380 *tsunami inundation model validation workshop*, pages 1–84. GeoClaw Tsunami Modeling Group University of Washington, 2011.
- 381 González, J., González, G., Aránguiz, R., Melgar, D., Zamora, N., Shrivastava, M. N., Das, R., Catalan, P. A., and Cienfuegos, R. A hybrid

- 382 deterministic and stochastic approach for tsunami hazard assessment in Iquique, Chile. *Natural Hazards*, 100:231–254, 2020.
- 383 Grezio, A., Babeyko, A., Baptista, M. A., Behrens, J., Costa, A., Davies, G., Geist, E. L., Glimsdal, S., González, F. I., Griffin, J., et al. Probabilistic  
384 tsunami hazard analysis: multiple sources and global applications. *Reviews of Geophysics*, 55(4):1158–1198, 2017.
- 385 Grilli, S. T., Harris, J. C., Tajalli Bakhsh, T. S., Masterlark, T. L., Kyriakopoulos, C., Kirby, J. T., and Shi, F. Numerical simulation of the 2011  
386 Tohoku tsunami based on a new transient FEM co-seismic source: Comparison to far-and near-field observations. *Pure and Applied  
387 Geophysics*, 170:1333–1359, 2013.
- 388 Hayes, G. P., Moore, G. L., Portner, D. E., Hearne, M., Flamme, H., Furtney, M., and Smoczyk, G. M. Slab2, a comprehensive subduction zone  
389 geometry model. *Science*, 362(6410):58–61, 2018.
- 390 Hill, E. M., Borrero, J. C., Huang, Z., Qiu, Q., Banerjee, P., Natawidjaja, D. H., Elosegui, P., Fritz, H. M., Suwargadi, B. W., Pranantyo, I. R., et al.  
391 The 2010 Mw 7.8 Mentawai earthquake: Very shallow source of a rare tsunami earthquake determined from tsunami field survey and  
392 near-field GPS data. *Journal of Geophysical Research: Solid Earth*, 117(B6), 2012.
- 393 Horspool, N., Pranantyo, I., Griffin, J., Latief, H., Natawidjaja, D., Kongko, W., Cipta, A., Bustaman, B., Anugrah, S., and Thio, H. A probabilistic  
394 tsunami hazard assessment for Indonesia. *Natural Hazards and Earth System Sciences*, 14(11):3105–3122, 2014.
- 395 Ichinose, G., Somerville, P., Thio, H. K., Graves, R., and O’Connell, D. Rupture process of the 1964 Prince William Sound, Alaska, earthquake  
396 from the combined inversion of seismic, tsunami, and geodetic data. *Journal of Geophysical Research: Solid Earth*, 112(B7), 2007.
- 397 Li, L., Switzer, A. D., Chan, C.-H., Wang, Y., Weiss, R., and Qiu, Q. How heterogeneous coseismic slip affects regional probabilistic tsunami  
398 hazard assessment: A case study in the South China Sea. *Journal of Geophysical Research: Solid Earth*, 121(8):6250–6272, 2016.
- 399 Mandli, K. T., Ahmadi, A. J., Berger, M., Calhoun, D., George, D. L., Hadjimichael, Y., Ketcheson, D. I., Lemoine, G. I., and LeVeque, R. J.  
400 Clawpack: building an open source ecosystem for solving hyperbolic PDEs. *PeerJ Computer Science*, 2:e68, 2016. doi: 10.7717/peerj-  
401 cs.68.
- 402 Melgar, D. Model output data for Alaska far-field tsunami simulations, 2025.
- 403 Melgar, D. and Hayes, G. P. Systematic observations of the slip pulse properties of large earthquake ruptures. *Geophysical Research Letters*,  
404 44(19):9691–9698, 2017.
- 405 Melgar, D., Williamson, A. L., and Salazar-Monroy, E. F. Differences between heterogenous and homogenous slip in regional tsunami hazards  
406 modelling. *Geophysical Journal International*, 219(1):553–562, 2019.
- 407 Melgar, D., Lin, T., Kong, Q., christineruhl, and Marfito, B. dmelgarm/MudPy: v1.3, Sept. 2021.
- 408 Mori, N., Takahashi, T., Yasuda, T., and Yanagisawa, H. Survey of 2011 Tohoku earthquake tsunami inundation and run-up. *Geophysical  
409 research letters*, 38(7), 2011.
- 410 Mori, N., Goda, K., and Cox, D. Recent process in probabilistic tsunami hazard analysis (PTHA) for mega thrust subduction earthquakes.  
411 *The 2011 Japan earthquake and tsunami: Reconstruction and restoration: Insights and assessment after 5 years*, pages 469–485, 2018.
- 412 Newman, A. V. and Okal, E. A. Teleseismic estimates of radiated seismic energy: The E/M 0 discriminant for tsunami earthquakes. *Journal  
413 of Geophysical Research: Solid Earth*, 103(B11):26885–26898, 1998.
- 414 NOAA, N. 2-minute gridded global relief data (ETOPO2) v2. *Natl Geophys Data Center, NOAA Natl Centers Env Inf*, 2006.
- 415 Okada, Y. Surface deformation due to shear and tensile faults in a half-space. *Bulletin of the seismological society of America*, 75(4):1135–  
416 1154, 1985.
- 417 Okada, Y. Internal deformation due to shear and tensile faults in a half-space. *Bulletin of the seismological society of America*, 82(2):1018–  
418 1040, 1992.

- 419 Powers, P. M., Altekruise, J. M., Llenos, A. L., Michael, A. J., Haynie, K. L., Haeussler, P. J., Bender, A. M., Rezaeian, S., Moschetti, M. P., Smith,  
420 J. A., et al. The 2023 Alaska National Seismic Hazard Model. *Earthquake Spectra*, 40(4):2545–2597, 2024.
- 421 Priest, G. R., Witter, R. C., Zhang, Y. J., Wang, K., Goldfinger, C., Stimely, L. L., English, J. T., Pickner, S. G., Hughes, K. L., Wille, T. E., et al.  
422 Tsunami inundation scenarios for Oregon. *Oregon Department of Geology Mineral Industries Open-File Report O-13*, 19, 2013.
- 423 Riquelme, S. and Fuentes, M. Tsunami efficiency due to very slow earthquakes. *Seismological Society of America*, 92(5):2998–3006, 2021.
- 424 Riquelme, S., Schwarze, H., Fuentes, M., and Campos, J. Near-field effects of earthquake rupture velocity into tsunami runup heights.  
425 *Journal of Geophysical Research: Solid Earth*, 125(6):e2019JB018946, 2020.
- 426 Sahakian, V., Melgar, D., and Muzli, M. Weak near-field behavior of a tsunami earthquake: Toward real-time identification for local warning.  
427 *Geophysical Research Letters*, 46(16):9519–9528, 2019.
- 428 Salazar-Monroy, E., Melgar, D., Jaimes, M., and Ramirez-Guzman, L. Regional probabilistic tsunami hazard analysis for the Mexican subduc-  
429 tion zone from stochastic slip models. *Journal of Geophysical Research: Solid Earth*, 126(6):e2020JB020781, 2021.
- 430 Satake, K. Mechanism of the 1992 Nicaragua tsunami earthquake. *geophysical research letters*, 21(23):2519–2522, 1994.
- 431 Sepúlveda, I., Liu, P. L.-F., and Grigoriu, M. Probabilistic tsunami hazard assessment in South China Sea with consideration of uncertain  
432 earthquake characteristics. *Journal of Geophysical Research: Solid Earth*, 124(1):658–688, 2019.
- 433 Sørensen, M. B., Spada, M., Babeyko, A., Wiemer, S., and Grünthal, G. Probabilistic tsunami hazard in the Mediterranean Sea. *Journal of*  
434 *Geophysical Research: Solid Earth*, 117(B1), 2012.
- 435 Suppasri, A., Imamura, F., and Koshimura, S. Effects of the rupture velocity of fault motion, ocean current and initial sea level on the  
436 transoceanic propagation of tsunami. *Coastal Engineering Journal*, 52(2):107–132, 2010.
- 437 Titov, V., Rabinovich, A. B., Mofjeld, H. O., Thomson, R. E., and González, F. I. The global reach of the 26 December 2004 Sumatra tsunami.  
438 *Science*, 309(5743):2045–2048, 2005.
- 439 UNDRR, C. *Economic losses, poverty & disasters: 1998-2017*. United Nations Office for Disaster Risk Reduction, 2018.
- 440 University of Washington Working Group. Probabilistic tsunami design maps for the ASCE 7-16 standard. In *ASCE 7-16 Tsunami Design Zone*  
441 *Maps for Selected Locations*, pages 1–17. American Society of Civil Engineers, Reston, VA, June 2017.
- 442 Williamson, A., Melgar, D., and Rim, D. The effect of earthquake kinematics on tsunami propagation. *Journal of Geophysical Research: Solid*  
443 *Earth*, 124(11):11639–11650, 2019.
- 444 Witter, R. C., Zhang, Y., Wang, K., Priest, G. R., Goldfinger, C., Stimely, L. L., English, J. T., and Ferro, P. A. Simulating tsunami inundation  
445 at Bandon, Coos County, Oregon, using hypothetical Cascadia and Alaska earthquake scenarios. *Oregon department of geology and*  
446 *mineral industries special paper*, 43:57, 2011.
- 447 Ye, L., Bai, Y., Si, D., Lay, T., Cheung, K. F., and Kanamori, H. Rupture model for the 29 July 2021 MW 8.2 Chignik, Alaska earthquake con-  
448 strained by seismic, geodetic, and tsunami observations. *Journal of Geophysical Research: Solid Earth*, 127(7):e2021JB023676, 2022.